ACS APPLIED MATERIALS & INTERFACES

Research Article

www.acsami.org

Balancing the Osteogenic and Antibacterial Properties of Titanium by Codoping of Mg and Ag: An in Vitro and in Vivo Study

Yaochao Zhao,[†,∥] Huiliang Cao,[‡,∥] Hui Qin,[†] Tao Cheng,[†] Shi Qian,[‡] Mengqi Cheng,[†] Xiaochun Peng,[†] Jiaxin Wang,[†] Yin Zhang,[†] Guodong Jin,[‡] Xianlong Zhang,[*,†] Xuanyong Liu,[*,‡] and Paul K Chu[§]

[†]Department of Orthopedics, Shanghai Sixth People's Hospital, Shanghai Jiao Tong University, Shanghai 200233, China

[‡]State Key Laboratory of High Performance Ceramics and Superfine Microstructure, Shanghai Institute of Ceramics, Chinese Academy of Sciences, Shanghai 200050, China

[§]Department of Physics and Materials Science, City University of Hong Kong, Tat Chee Avenue, Kowloon, Hong Kong China

Supporting Information

ABSTRACT: To simultaneously enhance the osteogenic and antibacterial properties of titanium, we introduced magnesium (Mg), silver (Ag), or both by using the plasma immersion ion implantation (PIII) technique, producing three PIII sample groups, namely, Mg-doped titanium (Mg−PIII), Ag-doped titanium (Ag−PIII), and Mg and Ag codoped titanium (Mg/Ag−PIII). The in vitro antibacterial efficacy of Mg/Ag−PIII group was about 7−10% higher than that of Ag−PIII. In vitro and in vivo results demonstrated that osteogenic property of Mg/Ag PIII group was better than that of Ag−PIII or Mg−PIII. It was believed that the galvanic effects between Mg and Ag NPs played a key role in facilitating the release of Mg but reducing the release of silver, answering for the selective performances of the Mg/Ag−PIII group over bacterial and mammalian cells. This study demonstrated that the integration of multiple functional elements could be realized by the dual-source PIII technique, and in this case, the antibacterial properties and osteogenic property of titanium could be balanced.

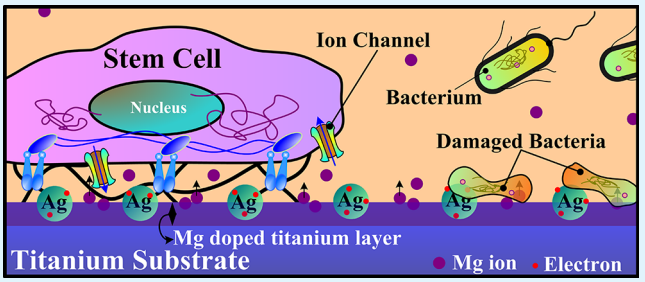

KEYWORDS: *silver nanoparticles, magnesium, antibacteria, osteogenesis, plasma immersion ion implantation*

1. INTRODUCTION

Titanium-based materials are widely used for implantable medical devices;[1] however, they still suffer from bacterial infections and lack of local tissue integration in vivo.[2] Coating of antimicrobial materials will reduce the infection rate of these devices, whereas it also may compromise the host actions in regeneration.[3] Hence, it is highly desired to balance the actions of titanium to bacterial and mammalian cells (e.g., for orthopedic and dental implants) to inhibit adhesion of pathogenic microbes while simultaneously promoting the adhesion of bone cells.[4]

Magnesium (Mg), at the early stage of osteogenesis, is capable of up-regulating the expression of integrins in bone cells, which is crucial to bone formation and metabolism.[5−7] It was evidenced that doping of Mg can promote the osteoblastic differentiation of human mesenchymal stem cells (hMSCs),[8] increase calcification,[9,10] and enhance mineral density of bone and osseointegration of the inserted implants.[11−14] On the other hand, silver (Ag) is famous for its biocidal activity against a broad spectrum of microbial and fungal species,[15,16] yet the human immune system is sensitive to the toxic effects rendered by free silver nanoparticles (Ag NPs), particularly at high concentrations.[17,18] Because of their small size and high mobility, Ag NPs can enter mammalian cells and undermine intracellular functions.[19−21] Therefore, restricting the mobility of Ag NPs is critical to clinical applications. Previously, we immobilized Ag NPs on titanium and stainless steel by silver plasma immersion ion implantation (Ag−PIII), and found the particles not only had good antibacterial activity but also possessed excellent cytocompatibility,[22−24] which was likely controlled by the galvanic corrosion effect.[24] However, the osteogenic property of Ag−PIII-treated titanium requires further improvement, and codoping of Mg and Ag may improve the performance of titanium. Although the bioeffect of Mg on the fate of mammalian cells and the antibacterial activity of silver have been carefully proved in numerous previous works as mentioned above, the codoping effects on biological performance of titanium were seldom concerned.

Previously, we preliminarily investigated the in vitro cellular responses to titanium successively treated by magnesium plasma immersion ion implantation (Mg−PIII) and silver plasma immersion ion implantation (Ag−PIII), and found that Mg and Ag had synergistic effect to some extent on improving both the antibacterial and osteogenic activities of titanium.[25]

Received: May 14, 2015
Accepted: July 23, 2015
Published: July 23, 2015

DOI: 10.1021/acsami.5b04168
ACS Appl. Mater. Interfaces 2015, 7, 17826−17836

However, the efficacy of this effect was highly influenced by the PIII parameters. Accordingly, in the present work, we systematically investigated the in vitro and in vivo biological properties of the Mg and Ag codoped titanium prepared by simultaneously triggering the Mg and Ag cathodic arcs for plasma immersion ion implantation (Mg/Ag−PIII).

2. MATERIALS AND METHODS

2.1. Samples Fabrication and Characterization. *2.1.1. Doping Procedures.* Cathodic arc sourced plasma immersion ion implantation (PIII) processes[26] were carried out for doping of silver (Ag), magnesium (Mg), or both on titanium surface. Three groups of PIII-treated samples were produced, designated as Mg−PIII (PIII at 30 kV for 1.5 h), Ag−PIII (PIII at 30 kV for 1.5 h), and Mg/Ag−PIII (PIII at 30 kV for 1.5 h). For Mg/Ag−PIII, both the Mg and Ag cathodes were simultaneously triggered. Other parameters were similar as detailed previously.[22,24] Commercially purchased (Cp) Ti (Grade 2) was used as substrate in all the sample groups (the blank Ti and the PIII-treated Ti). Before evaluation or before PIII treatments, Cp Ti was pretreated in a 5 wt % oxalic acid solution at 100 °C for 2 h and ultrasonically cleaned with distilled water.

2.1.2. Material Characteristics. The surface morphologies of the concerned sample groups were examined by using a field-emission scanning electron microscopy (FE-SEM; S-4800, HITACHI, Japan). The chemical states and depth profiles of the doping compositions (Ag and Mg) were evaluated by using the X-ray photoelectron spectroscopy (XPS; PHI 5802, Physical Electronics Inc., Eden Prairie, MN). The dynamic potential polarization curves were determined under the CHI760c electrochemical workstation (CHI Instruments, Inc., Shanghai) by soaking the samples in a 0.9% NaCl solution (pH = 7) at room temperature.

2.1.3. Release of Doped Materials. The PIII-treated titanium samples (2 cm squares) were immersed in 10 mL of PBS (phosphate buffer solution) for various durations (7, 14, 21, and 28 days) at 37 °C without agitating. The resultant solutions (containing Mg, Ag, or Mg/Ag) were analyzed by using the inductively coupled plasma atomic emission spectroscopy (ICP-AES).

2.2. In Vitro Cytocompatibility. *2.2.1. Culture and Expansion of hBMSCs.* Human bone marrow mesenchymal stem cells (hBMSCs), which were acquired from Stem Cell Bank of Chinese Academy of Science, were expanded in MEM alpha medium (α-MEM; Gibco, GB) containing 10% fetal bovine serum (FBS; Hyclone, Logan, UT) and 1% antibiotic/antimyotic solution (Antibiotic-Antimycotic, Hyclone, Logan, UT). Cells were cultured at 37 °C in an environment of 5% CO_2 and passaged every 3 days. Only confluent hBMSCs at passage 3−5 were harvested for further study.

To assess early cell adhesion and cytoskeleton characteristics, we introduced the hBMSCs suspension with a concentration of 5.0×10^4 cells per well on the sample surfaces. For the evaluation of proliferation and morphology, cells were added on the specimens at a density of 1.0×10^4 cells per well. In alkaline phosphatase (ALP) quantification, extracellular matrix mineralization, and real-time reverse-transcriptase polymerase chain reaction (Real-time RT-PCR) measurements, cells were cocultured with different specimens at a density of 1.0×10^4 cells per well (7 days) and 0.5×10^4 cells per well (14 days).

2.2.2. Early Cell Adhesion and Cytoskeleton Characteristics. To assess early cell adhesion and cytoskeleton property, we carried out DAPI and rhodamine phalloidin staining. The cells, at different culture times (1, 8, and 24 h), were washed with the phosphate buffer saline (PBS) (pH = 7.4) three times. Then, the samples were fixed in 4% paraformaldehyde for 10 min at room temperature. Cell membranes were permeated by Triton X-100 (0.1% v/v) for 2 min, and then, rhodamine phalloidin (Sigma, St. Louis, MO) and DAPI (Sigma, St. Louis, MO) were prepared and coincubated with the cells at 37 °C in darkness for 1 h and 5 min, respectively. Fluorescence microscopy (Olympus, Japan) was used to observe the F-actin and cell nuclei.

2.2.3. Cell Proliferation. Cell proliferation was evaluated by Cell Counting Kit-8 assay (CCK-8, Beyotime) after the cells cocultured with various samples for 1, 4, and 7 days. Briefly, after the cells were cultured onto each sample for the prescribed culturing period, the samples were shifted to another new 24-well plate. Then, fresh medium and CCK-8 solution with a ratio of 10:1 was added into each well and incubated at 37 °C for 4 h. After incubation, 100 μL of the suspension was introduced to a 96-well plate, and the absorbance was read at 450 nm.

2.2.4. Cell Morphology. Scanning electron microscopy (SEM) was applied to observe the cell morphology and specifics of cell/biomaterial interaction. The samples with the attached hBMSCs were fixed with 2.5% glutaraldehyde at each time point. Then, they were dehydrated in graded ethanol series (30, 50, 75, 90, 95, and 100 v/v %), freeze-dried, sputter coated with platinum, and observed by SEM.

2.2.5. Alkaline Phosphatase Activity Assay. For alkaline phosphatase (ALP) staining, the fixed cells by citrate buffered acetone at the prescribed time points were incubated in a solution consisting of fast blue RR salt (Sigma-Aldrich) and naphthol AS-MX phosphate (Sigma-Aldrich) for 30 min. Afterward, the samples were treated with Mayer's Hematoxylin reagent (Sigma-Aldrich) for 10 min. Images were taken by fluorescence microscopy (OLYMPUS, Japan).

The ALP activity was evaluated by ALP reagent. The cells were disassociated by the alkaline lysis buffer from the samples. Then, lysates were reacted with p-nitrophenyl phosphate (Sigma) at 37 °C for 30 min for the colorimetric analysis. The optical density (OD) values of the resulting solution were measured at a wavelength of 405 nm. At last, the ALP levels were normalized to the total intracellular protein content determined using the BCA protein assay. The experiments were performed three times.

2.2.6. Extracellular Matrix Calcium Deposition Assay. Alizarin red staining assay was employed to evaluate extracellular matrix (ECM) calcium deposition. After 7 and 14 days, the hBMSCs were fixed in 70% ethanol for 1 h. Then, the specimens were stained with 40 mM Alizarin Red S for 10 min. The unbound red residue was rinsed with PBS, and snapshots were taken by optical microscopy. The bound stain was eluted using 10% cetylpyridinium chloride in 10 mM sodium phosphate (pH 7.0), and the OD values of the resulting solution were measured at 600 nm. The measurements were repeated three times.

2.2.7. Osteogenic Gene Expression. Human BMSCs osteogenic differentiation was determined by the expression levels of osteogenesis-related genes, which were measured using the real-time reverse-transcriptase polymerase chain reaction (real-time RT-PCR). After 7 and 14 days, the RNA was extracted using TRIzol reagent (Invitrogen). Briefly, the constructs were washed with PBS, immersed in Trizol, and vigorously shaken to lyse the cells. Proteins separation was performed using chloroform. RNA was recovered using isopropanol and precipitated by alcohol.

Afterward, complementary first strand DNA (cDNA) was synthesized from total RNA using PrimeScript RT reagent Kit (Takara) according to the manufacturer's protocol. Briefly, a reaction mixture consisting of PrimeScript Buffer, PrimeScript RT Enzyme Mix I, Oligo dT Primer, Random 6 mers, 300 ng of total RNA and RNase free dH_2O (double distilled H_2O) was prepared in a tolal volume of 20 μL. The single-strand cDNA was synthesized by incubating the complete reaction mixture for 15 min at 37 °C, followed by incubation at 85 °C for 5 min.

RT-PCR analysis was operated on the Bio-Rad C1000 using SYBR Premix Ex TaqII (Takara). The target cDNA for real-time PCR quantification was amplified according to manufacturer's recommendations. Briefly, a PCR mixture consisting of SYBR Premix Ex TaqII, primer, cDNA solution and dH_2O was prepared in a final volume of 25 μL. Forty cycles of denaturation, annealing, and extension were carried out on the Bio-Rad C1000 for all genes. The expression level of the housekeeping gene GAPDH was used to normalize that of the target genes and the relative quantification calculated by the ΔCT method. The primers for the target genes are listed in Table 1.

2.3. Antibacterial Assay. *Escherichia coli* (ATCC 25922) and *Staphylococcus aureus* (ATCC 43300) were used to assess the antibacterial effect of the various samples. In this study, we assessed the activity of the PIII-treated groups (Mg−PIII, Ag−PIII, Mg/Ag

DOI: 10.1021/acsami.5b04168
ACS Appl. Mater. Interfaces 2015, 7, 17826−17836

Table 1. Primers for RT-PCR

gene	prime sequence (F, forward; R, reverse; 5′−3′)	product size (bp)
RUNX2	F: GAGATCATCGCCGACCAC	135
	R: TACCTCTCCGAGGGCTACC	
ALP	F:CCGTGGCAACTCTATCTTTGG	79
	R:GCCATACAGGATGGCAGTGA	
OCN	F:AGCAAAGGTGCAGCCTTTGT	63
	R:GCGCCTGGGTCTCTTCACT	
Col-1	F:AGGGCCAAGACGAAGACATC	138
	R:AGATCACGTCATCGCACAACA	
GAPDH	F:ATGGGGAAGGTGAAGGTCG	119
	R:TAAAAGCAGCCCTGGTGACC	

PIII) against planktonic and adherent bacteria and found the samples had no apparent antibacterial effect on the planktonic microbes (Figure S1). So, the following studies mainly focused on the antibacterial ability of the samples against the adherent bacteria. Live/Dead staining and bacterial counting method were carried out as follows: 100 μL of diluted bacterial solution at a density of 10^7 CFU ml^{-1} was dropped onto the sterilized sample. The samples with the bacterial solution were incubated at 37 °C for 24 h and then stained according to the illustration of the LIVE/DEAD BacLight bacteria viability kits (L13152, Invitrogen). In brief, one Component A pipet (containing yellow-orange solids) and one Component B pipet (containing red solids) were dissolved in filter-sterilized dH_2O to prepare a stock solution of the LIVE/DEAD BacLight staining reagent mixture. Then, 500 μL of staining reagent mixtures was added to the surface of the samples and incubated in darkness for 15 min at room temperature. Before this, the samples were rinsed twice slightly with PBS. At last, the samples were shifted to a coverslip and detected by a fluorescence microscopy.

The specimens with 1 mL of the bacteria-containing medium (10^7 CFU ml^{-1}) were cultured on 24-well culture plates at 37 °C for 24 h. The bacteria on the surface of the samples were ultrasonically detached in 5 mL of the PBS solution for 5 min. Afterward, bacterial solution was diluted successively using 10-fold dilution method. Then, 200 μL of diluted bacterial solution was spread on an agar culture plate. After 24 h of incubation, the live bacteria count was performed in accordance with the National Standard of China GB/T 4789.2 protocol. Then, the antibacterial ratio was measured based on the following formulas: antibacterial rate (%) = (CFU of control − CFU of experimental groups)/CFU of control × 100, where pure Ti served as the control and Mg−PIII, Ag−PIII, and Mg/Ag−PIII constituted the experimental groups.

For the SEM examination, a drop of bacterial suspension (10^7 CFU ml^{-1}) was dripped on the samples. After incubation for 24 h, the samples with the attached bacteria were fixed with 2.5% glutaraldehyde, dehydrated in a graded ethanol series for 10 min, freeze-dried, sputter coated with platinum, and observed by SEM.

2.4. In Vivo Evaluation. *2.4.1. Animals and Surgery.* All the animal surgeries described in this paper followed the requirements of the Animal Care and Experiment Committee of Sixth People's Hospital affiliated with the school of Medicine of Shanghai Jiaotong University. Six male New Zealand white rabbits weighing 3000 ± 400 g (average age, 8 months) were used in the experiments. The surgery was performed under standard sterile surgical conditions. The rabbits were anaesthetized with 0.9 mL of 3% pentobarbital sodium solution per 1000 g by intravenous injection before surgery. The operation site was shaved and sterilized. Then, the left tibia shaft was exposed by the medial approach. A kirschner wire with a diameter of 2.0 mm was used to drill four parallel holes from the proximal to distal part with intervals at 1 cm. The sterile ion-implanted rods with a diameter of 2.0 mm and length of 7 mm were knocked randomly into four holes, and the wound was closed carefully. After the operation, all the rabbits received subcutaneous injection of gentamycin as an antibiotic prophylaxis, and they were kept under specific pathogen free (SPF) conditions with free access to water and food.

2.4.2. Sequential Fluorescent Labeling Assay. A polychrome sequential fluorescent labeling method was employed to label the new bone formation over time. At 2, 4, and 6 weeks after operation, three types of fluorochromes were injected intraperitoneally in a sequence of 25 mg/kg tetracycline hydrochloride (TE; Sigma), 30 mg/kg Alizarin Red S (AL; Sigma), and 20 mg/kg Calcein (CA; Sigma), respectively.

2.4.3. Sample Harvest and Fixation. Eight weeks after surgery, the rabbits were euthanized, and the left tibias with the implants were harvested and sawed into the suitable size. The samples were fixed in 10% buffered formaldehyde for further analysis.

2.4.4. Micro-CT Evaluation. The prepared samples were scanned using Micro-CT (Skyscan 1172, Bruker Micro-CT, Germany) to assess the changes in the bone tissues around the implants. Scanning was performed at a maximum X-ray energy and over 360° at 50 kV and 200 μ with a resolution of 18 μm. Three-dimensional (3D) images were rebuilt by NRecon (Skyscan Company, Bruker micro CT, Germany). The 3D models were generated by CTVol (Skyscan Company, Bruker micro CT, Germany) and analyzed using the CTAn

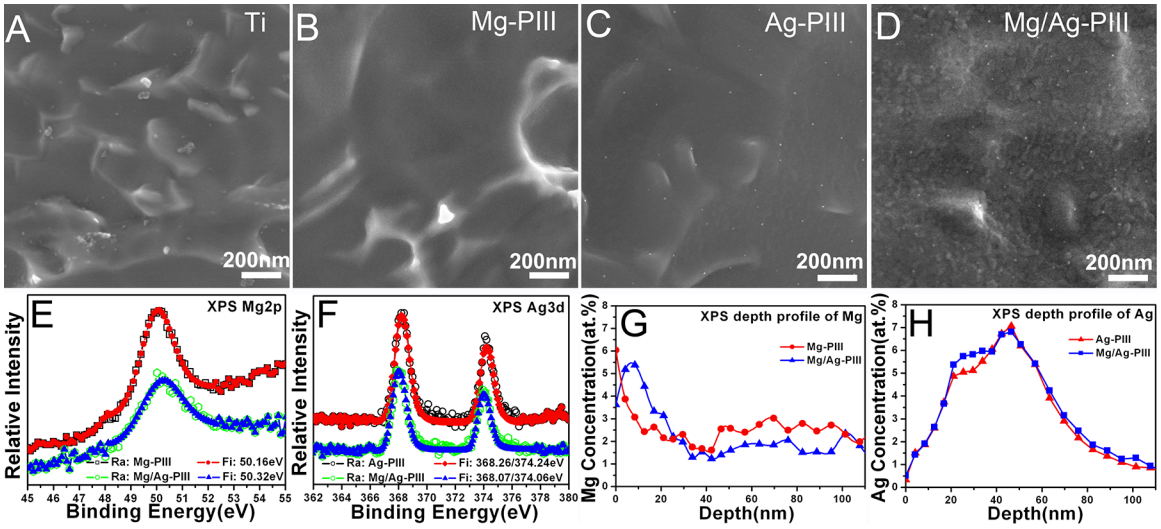

Figure 1. Scanning electron microscopy (SEM) images of the titanium samples before and after PIII: (A) Ti, (B) Mg−PIII, (C) Ag−PIII, (D) Mg/Ag−PIII. XPS spectra: (E) XPS Mg 2p, (F) XPS Ag 3d, (G) XPS depth profile of Mg, and (H) XPS depth profile of Ag. Ra represents the raw intensity; Fi represents the fitted intensity.

DOI: 10.1021/acsami.5b04168
ACS Appl. Mater. Interfaces 2015, 7, 17826−17836

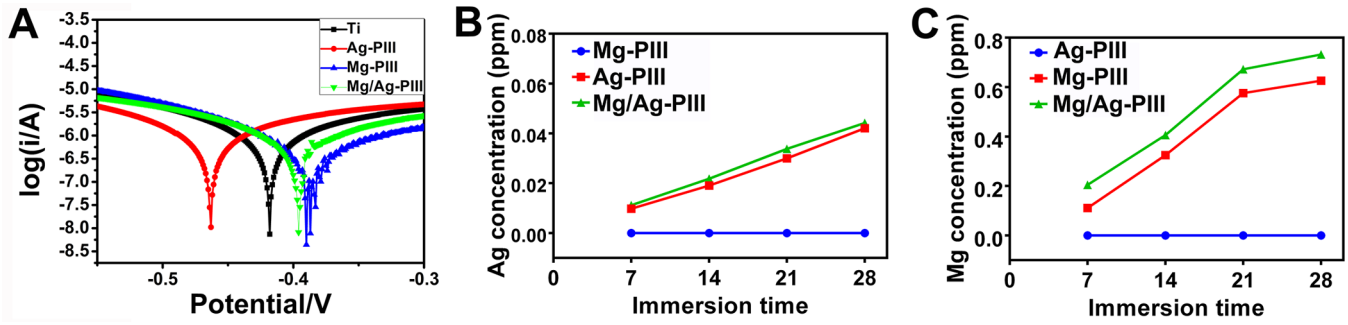

Figure 2. (A) Potentiodynamic polarization curves, (B) and (C) show the Ag and Mg concentrations released from a 2 × 2 cm sample immersed in PBS at different time points (7, 14, 21, and 28 days).

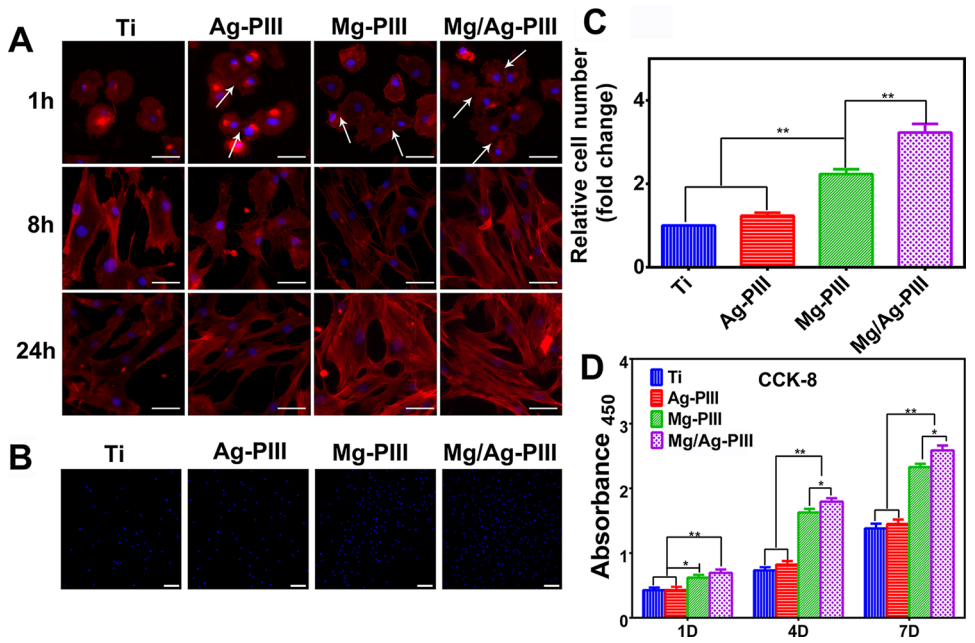

Figure 3. (A) Cytoskeletons of human mesenchymal stem cells (hBMSCs) seeded on various samples were stained with rhodamine phalloidin (red), and nuclei were stained with DAPI (blue) at prescribed time points (1, 8, and 24 h). The size bar represents 50 μm. (B) Adhered hMSCs on various samples were stained with DAPI (bar = 100 μm) after 1 h of culture and (C) the relative number was calculated. (D) Cell proliferation was measured by CCK-8 after 1, 4, and 7 days of culture; $^{*}P < 0.05$,$^{**}P < 0.01$.

program (Skyscan Company, Bruker Micro-CT, Germany). The surrounding area of the implants with a radius of 0.5 mm within the bone marrow cavity was chosen to quantify the new bone formation. The bone mineral density (BMD) and bone volume fraction (bone volume/total volume, BV/TV) of new bone were analyzed.

2.4.5. Histological Observation. After being scanned by Micro-CT, the tibia samples were dehydrated in gradient ethanol solution (70, 80, 90, 95, and 100 v/v %), and embedded in polymethylmetacrylate (PMMA).[27] Leica SP1600 saw microtome (Leica, Hamburg, Germany) was used to cut the embedded specimens into 150 μm thick transverse sections. Sandpapers with increased grit size were used to ground and polish those sections to a final thickness of about 50 μm. Then, the polished samples were observed under confocal laser scanning microscope (CLSM, Leica). excitation and emission wavelengths of chelating fluorochromes were used 405/560−590, 543/580−670, and 488/500−550 nm for tetracycline hydrochloride (yellow), alizarin red S (red), and calcein (green), respectively.[28] Then, the sections were stained with van Gieson's picrofuchsin for histological observation.

2.5. Statistical Analysis. The statistical assessment was performed using Statistical Package for the Social Sciences version 18 software (SPSS, Chicago, IL). The data were expressed as mean ± SD. To determine the statistical significance of observed differences between the study groups, we applied one-way or two-way ANOVA followed by Bonferroni post-hoc tests based on normality distribution (Kolmogorov−Smirnov test with Lilliefors' correction) and equal variance testing (Levene median test). The statistical significance was defined as $p < 0.05$.

3. RESULTS

3.1. Surface Characterization. The surface microstructures of the plasma-treated and untreated titanium samples were observed by SEM. Compared to the flat topography of the pure titanium sample (Figure 1A), no new nanostructure was produced on Mg−PIII (Figure 1B) but uniformly distributed particles about 5 nm in diameter were observed on Ag−PIII (Figure 1C) and Mg/Ag−PIII (Figure 1D). There were more particles on Mg/Ag−PIII than that on Ag−PIII. This trend was different from that previously observed on titanium which was successively treated with magnesium and silver.[25] It is believed that the difference stemmed from knock-on collisions and interactions between the energetic atoms (Mg and Ag atoms in present study) in dual-source metal plasma immersion ion implantation,[29] which enhanced the nucleation rate of silver particles. In addition, both the Ag−PIII and Mg/Ag−PIII

DOI: 10.1021/acsami.5b04168
ACS Appl. Mater. Interfaces 2015, 7, 17826−17836

groups had nanoparticles, but the Mg−PIII group did not. This phenomenon is mainly determined by the thermochemistry of titanium substrate and the doping materials (Mg and Ag) and the temperature of the system (resulted from the bombing of the energetic Mg or Ag atoms),[30] which further resulted in the distinct behaviors of Mg and Ag in wettability.[31]

To reveal the chemical states of the doped elements in titanium, we analyzed the Mg and/or Ag implanted samples by X-ray photoelectron spectroscopy (XPS). As shown in Figure 1E, the Mg 2p peak at about 50.2 eV acquired from Mg−PIII and Mg/Ag−PIII corresponds to magnesium oxide.[32] The Ag 3d doublet at about 368.1 eV/374.1 eV (Figure 1F) corresponds to the metallic silver, indicating that the particles observed on Ag−PIII were metallic silver.[33−35] As shown in Figure 1G,H, the Mg concentration in Mg−PIII decreased gradually from the surface with the highest concentration of 6.0 atomic percent (atom %), while the Mg content at the surface was not the highest in Mg/Ag−PIII, the peak concentration was about 5.5 atom % at the depth of 10 nm. The integrated concentration calculated by area under curve (AUC) based on the profile of Mg in the Mg−PIII (AUC = 291) was slightly higher than that in Mg/Ag−PIII (AUC = 250). On the other hand, the silver concentration on the surface of Mg/Ag−PIII was 0.5 atom %, which was higher than that of Ag−PIII (0.3 atom %); therefore, more silver particles were observed on Mg/Ag−PIII than on Ag−PIII. Silver peaks (about 7.3 atom %, located at about the depth of 50 nm) were formed at about the same depths in Ag−PIII and Mg/Ag−PIII, and the integrated concentrations of silver demonstrated that the total amounts of silver (AUC = 401) in Ag−PIII and Mg/Ag−PIII (AUC = 412) were about the same. In addition, as indicated by the XPS results (Figure 1G,H), the ratio of Mg/Ag on the surface of Mg/Ag−PIII was about 7:1.

In addition, the dynamic potential polarization curves of the samples were tested in 0.9% NaCl. As shown in Figure 2A, in comparison to the Ti control, the corrosion potentials (E_{cor}) of Ag−PIII shift to the negative side, while those of Mg−PIII and Mg/Ag−PIII shift positively indicating that the latter two groups had better corrosion resistance. The amounts of Mg and Ag leached from the PIII treated samples were determined by ICP-AES, the results indicated that the Ag release from Mg/Ag−PIII and Ag−PIII were approximately equal (Figure 2B), while the Mg released from Mg/Ag−PIII was significantly more (nearly twice) than that from Mg−PIII after immersion for 7 days or longer (Figure 2C). The positive shift in the corrosion potential and larger amount of Mg leached from Mg/Ag−PIII (compared to Mg−PIII) suggested that microgalvanic couples of Mg/Ag were likely formed in Mg/Ag−PIII.

3.2. Response of hBMSCs. The cytoskeleton (F-actin) and nuclei of the hBMSCs seeded on the different surfaces were stained with rhodamine phalloidin and DAPI respectively, and the images were displayed in Figure 3A. In the first hour, the hBMSCs on all the groups exhibited an irregular spherical morphology, yet the cells on Mg−PIII and Mg/Ag−PIII present more filopodia, indicating better spreading of the cells on these samples (more obvious on Mg/Ag−PIII). In addition, compared to the pure Ti control, more mitotic phases were detected on the plasma-treated surfaces within 1 h (marked by white arrows in Figure 3A), especially on Mg/Ag−PIII. The relative number of adherent cells shown the following trend: Mg/Ag−PIII > Mg−PIII > Ag−PIII > Ti (Figure 3B,C). These results indicated that Mg promoted the initial spreading of hBMSCs. After culturing for 8 h, the superiority of Mg PIII over the pure Ti control and Ag PIII became more apparent. The cells on the Mg/Ag−PIII and Mg−PIII surfaces demonstrated an orderly multipolar spindle shape, whereas the polygonal cells with a fuzzy cytoskeleton were detected on the pure Ti and Ag−PIII (Figure 3A), suggesting that the cells adapt quickly on the Mg−PIII surface. The F-actin structure was still different significantly after 24 h incubation (Figure 3A). More filopodia and lamellipodia were detected on Mg−PIII and Mg/Ag−PIII than that on pure Ti and Ag−PIII. Proliferation of hBMSCs was further assessed by the CCK-8 assay. As shown in Figure 3D, proliferation rates of hBMSCs on pure Ti and Ag-doped titanium were lower than those on Mg- and Mg/Ag-doped surfaces. The cells on Ag−PIII exhibited a slightly higher proliferation, suggesting that Ag−PIII had low cytotoxicity. Furthermore, the hBMSCs on Mg/Ag PIII showed relatively higher proliferation than that on Mg−PIII, especially after the fourth and seventh days. This trend was likely related to the larger Mg release from Mg/Ag−PIII, as shown in Figure 2C.

The cell morphology on the samples was further observed by SEM, as shown in Figure 4, after culturing for 1 day, the cells

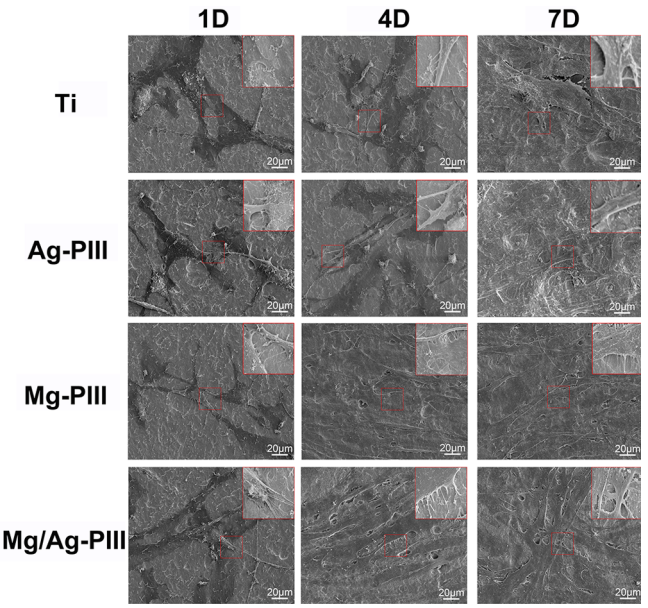

Figure 4. Morphology of hBMSCs on various surfaces determined by scanning electron microscopy (SEM) after 1, 4, and 7 days of culture and (insets) magnified sections showing the filopodia and connections between cells.

extend well on all the samples, yet the cells on Mg−PIII and Mg/Ag−PII presented more filopodia. At day 4, the trend was more apparent, compared to the monolayer of cells on Ti and Ag−PIII, the clustered cells formed a multilayered structure and covered most of the surface on Mg−PIII and Mg/Ag−PIII. At day 7, stacked cells were observed on all the groups, and the cells on Mg−PIII and Mg/Ag−PIII treated surfaces were interconnected better.

The ALP activity of the hBMSCs cultured on various surfaces was evaluated by the ALP staining kit at days 7 and 14. As shown in Figure 5A, Mg−PIII and Mg/Ag−PIII displayed larger stained areas than pure Ti and Ag−PIII, and Mg/Ag−PIII was the best. The trend was consistent with results obtained via the quantitative assay, as shown in Figure 5B. Moreover, the ECM calcium deposition area is larger on Mg/

DOI: 10.1021/acsami.5b04168
ACS Appl. Mater. Interfaces 2015, 7, 17826−17836

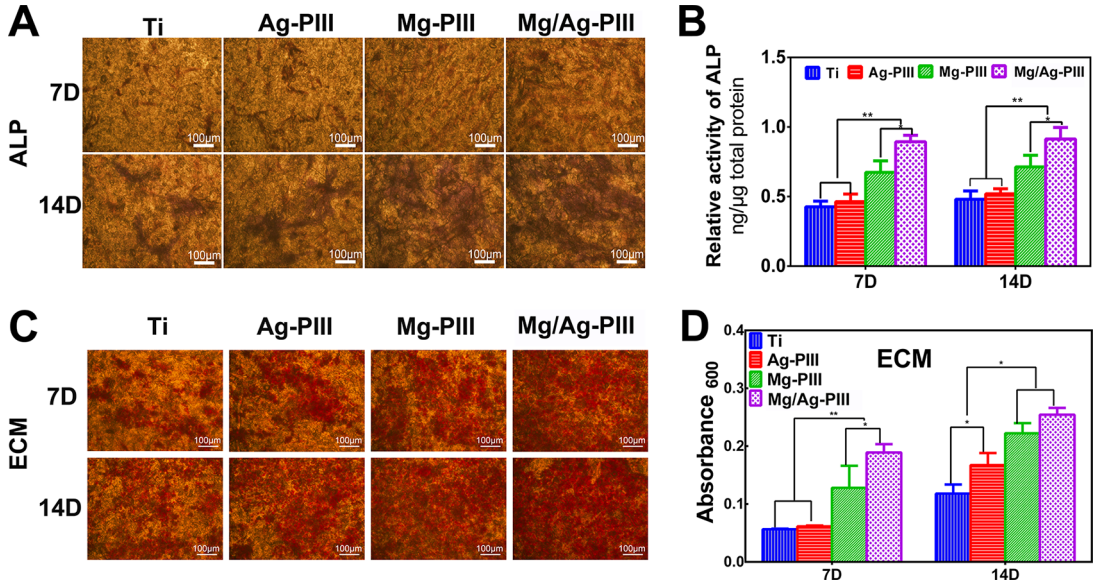

Figure 5. (A) Alkaline phosphatase (ALP) staining of hBMSCs and (B) corresponding optical density (OD) values after 4 and 7 days of culture on various surfaces. Calcium deposition determined by alizarin red staining: (C) the stained area on various surfaces for 7 and 14 days, and (D) corresponding OD values; $*P < 0.05$, $**P < 0.01$.

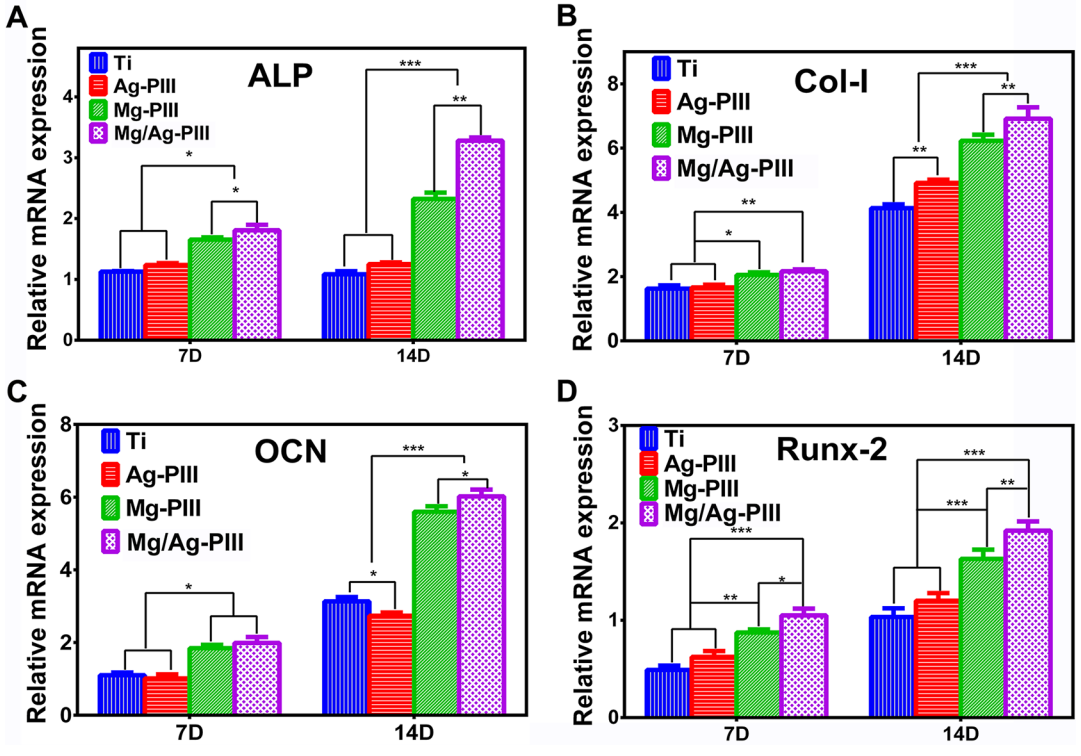

Figure 6. Osteogenic gene expression of hBMSCs after 7 and 14 days of culture on various surfaces: (A) ALP, (B) Col-I, (C) OCN, and (D) Runx2; $*P < 0.05$, $**P < 0.01$, $***P < 0.001$.

Ag−PIII and Mg−PIII than that on Ti and Ag−PIII (Figure 5C). It was further confirmed by the quantitative trend shown in Figure 5D.

The expression of the genes related to osteogenesis, including Runx2, ALP, OCN, and Col-I, in the cells cultured on pure Ti, Ag−PIII, Mg−PIII, and Ag/Mg−PIII for 7 and 14 days were quantified by real-time PCR, and the results are shown in Figure 6. The PIII samples, to some extent, up-regulated all the concerned genes in hBMSCs. After incubation for 7 days, the cells on Mg/Ag−PIII expressed the highest mRNA level of ALP and Runx2 among the four groups. It should be noted that the expressions of Runx2, ALP, OCN, and Col-I mRNA were significantly higher on Mg−PIII and Mg/Ag−PIII than those on the other two groups. At day 14, the cells on Mg/Ag−PIII expressed the highest mRNA levels of Runx2, ALP, OCN, and Col-I, followed by Mg−PIII. The expressions of ALP and Col-I on Ag−PIII were also higher than that on pure Ti.

DOI: 10.1021/acsami.5b04168
ACS Appl. Mater. Interfaces 2015, 7, 17826−17836

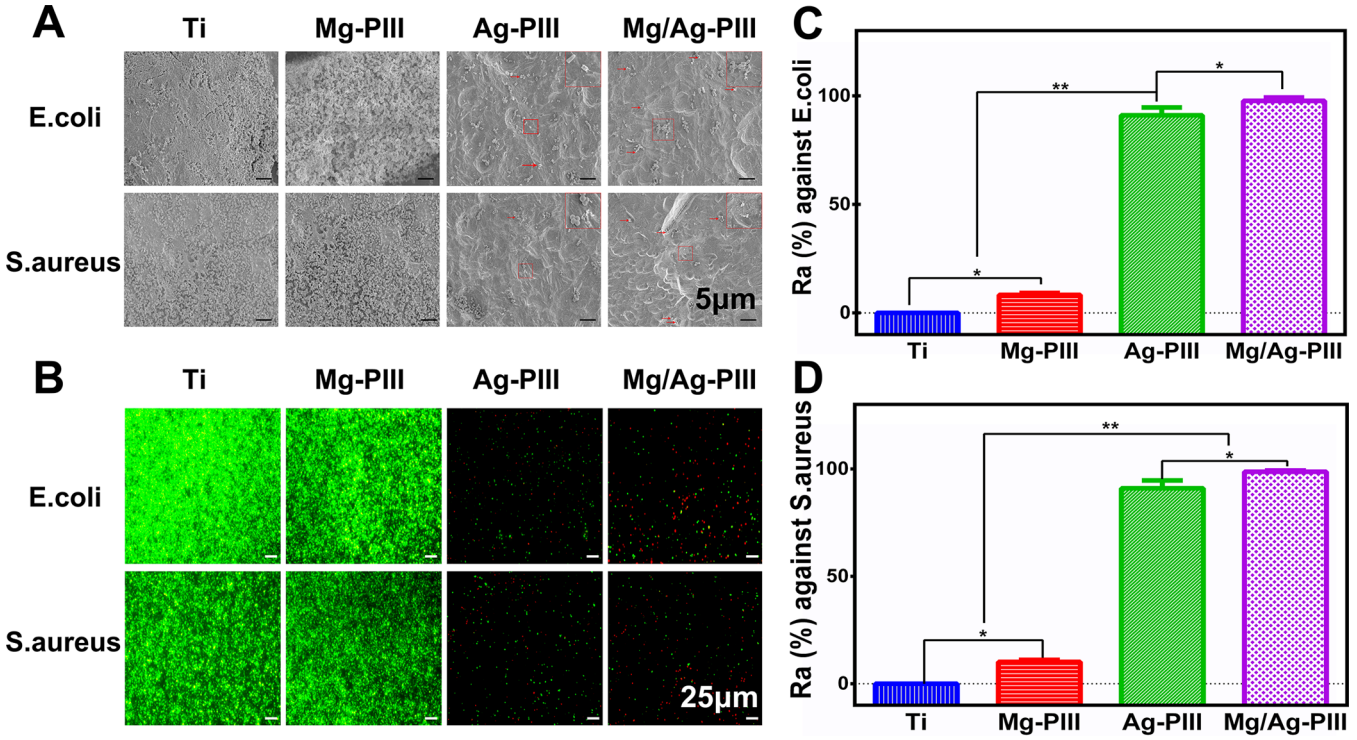

Figure 7. Antibacterial property of the samples after 24 h of incubation with bacteria (10^7 CFU/ml) was evaluated by SEM, Live/Dead staining and spread plate method: (A) SEM images of various surfaces; (B) fluorescent images of *S. aureus* and *E. coli*, live cells were stained green and dead cells were stained red; (C) antibacterial rates (Ra) of the samples against *E. coli*; (D) antibacterial rates (Ra) of the samples against *S.aureus*; $^*P < 0.05$, $^{**}P < 0.01$.

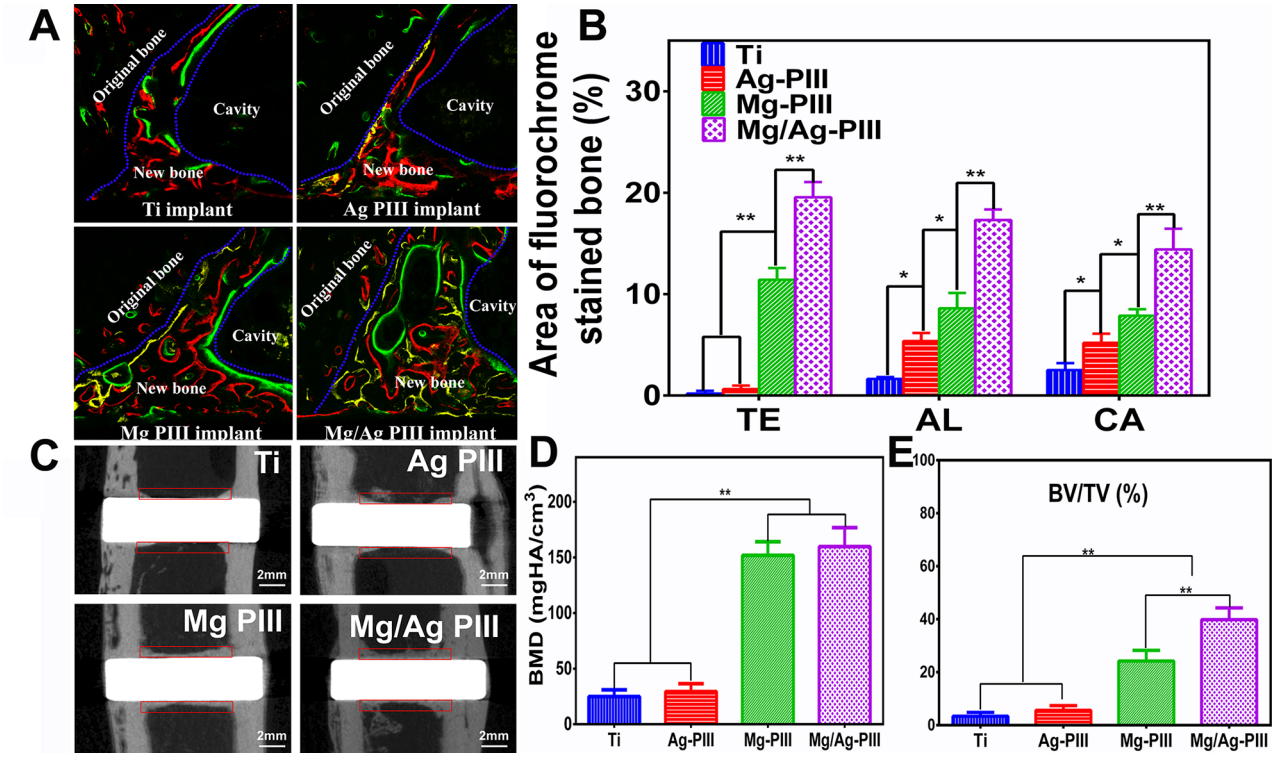

Figure 8. New bone formation over time determined by polychrome sequential fluorescent labeling method: (A) new bone (between blue dashed line) stained with yellow (tetracycline hydrochloride, TE), red (Alizarin Red S, AL) and green (Calcein, CA), respectively (bar = 100 μm). (B) Corresponding areas of different fluorochromes. The typical central coronal sections of the rabbit tibias with implants after 6 weeks were reconstructed and analyzed by Micro-CT: (C) Micro-CT images of the coronal sections; new bone areas were marked by red rectangles; (D) bone mineral density (BMD) of the new bone; (E) bone volume fraction (bone volume/total volume, BV/TV) of the new bone; ($^*P < 0.05$, $^{**}P < 0.01$).

DOI: 10.1021/acsami.5b04168
ACS Appl. Mater. Interfaces 2015, 7, 17826−17836

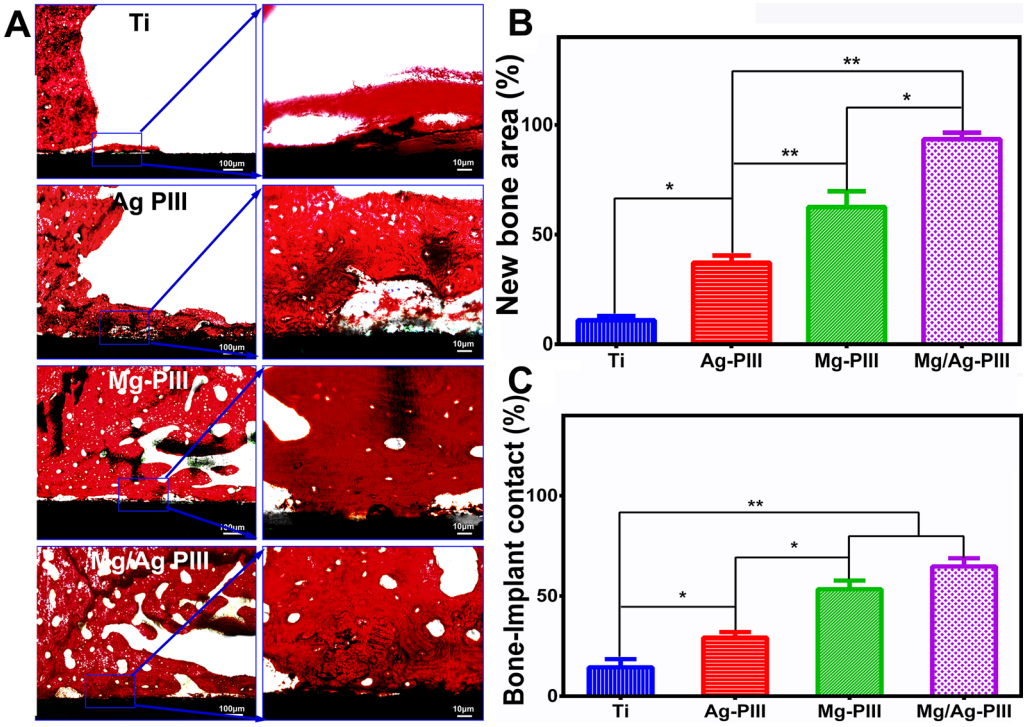

Figure 9. Histological sections were stained by van Gieson's picrofuchsin staining assay and analyzed by the histomorphometric measurements: (A) van Gieson's picrofuchsin staining sections. Higher magnifications of the blue rectangle area were displayed in the right panel. (B) Percentage of new bone area. (C) Percentage of bone/implant contact (BIC); (*$P < 0.05$, **$P < 0.01$).

3.3. In Vitro Antibacterial Ability. The antibacterial property of the samples was evaluated by SEM, Live/Dead staining and spread plate method. The SEM images of *E. coli* and *S. aureus* are shown in Figure 7A. After culturing on Ti and Mg−PIII for 24 h, the bacteria cells on the Ti control conglomerated into grape-like colonies and formed a wide-range biofilm, whereas only a few adherent bacteria were observed on Ag−PIII and Mg/Ag−PIII. Moreover, the adherent bacterial cells on these two groups were in distorted morphologies, and some of them were completely lysed, especially on Mg/Ag−PIII. A similar trend was observed in Live/Dead staining. As shown in Figure 7B, after culturing for 24 h, the green fluorescent intensity (live bacterial colonies) decreased, and the red fluorescent intensity (dead bacterial colonies) increased among the groups according to the following sequence: Ti, Mg−PIII, Ag−PIII, and Mg/Ag−PIII. Red spots were hardly observed on Ti and Mg−PIII; conversely, more red spots were present on Ag−PIII and Mg/Ag−PIII, demonstrating that a synergistic antibacterial effect of Mg/Ag−PIII on the adherent bacteria. The antibacterial rate (Ra) was evaluated by a spread plate method, as shown in Figure 7C,D; the Ra values of *E. coli* on Mg−PIII, Ag−PIII, and Mg/Ag−PIII are 8, 88, and 97% respectively; and those of *S. aureus* on Mg−PIII, Ag−PIII, and Mg/Ag−PIII were 10, 92, and 99%, respectively.

3.4. In Vivo Osseointegration. To evaluate the formation process of new bone, we studied the interfaces of bone and the indwelled implants. Three types of fluorochrome were used to label the new bone areas at prescribed time points. Generally, as shown in Figure 8A, the Mg−PIII and Mg/Ag−PIII groups, compared to the pure Ti and Ag−PIII, were apparently better at promoting new bone formation and mineralization at the bone-implant interface. At week 2, the percentages of yellow area labeled by tetracycline hydrochloride (Figure 8B) for Ti, Ag−PIII, Mg−PIII, and Mg/Ag−PIII were 0.2 ± 0.27, 0.64 ± 0.33, 11.42 ± 1.15, and 19.56 ± 1.50%, respectively. Apparently, more bone labeled by yellow can be observed on the Mg/Ag−PIII implant surface, which indicates better osteogenic ability of titanium treated by Mg/Ag at an early stage. At week 4, the percentage of red area labeled by Alizarin Red S for Mg/Ag−PIII (17.3 ± 1.1%) was larger than that of Mg−PIII (8.6 ± 1.51%, $p < 0.01$), and both of them were larger than those of pure Ti (5.4 ± 0.8%) and Ag−PIII (1.64 ± 0.18%). Another notable result was that Ag−PIII also promoted the formation of bone as the time prolonged. A similar tendency was observed at week 6, and the percentage of green area labeled by Calcein for Mg/Ag−PIII was 14.4 ± 2.1% which was the largest among the four sample groups.

The typical reconstructed central coronal sections of the implants by Micro-CT were displayed in Figure 8C, and the new bone area was marked by red rectangles. The bone volume around Mg/Ag−PIII was bigger than that of the other samples. In comparison to pure Ti and Ag−PIII groups, the new bone formed a bridge connecting both sides of the medullary cavity on Mg−PIII and Mg/Ag−PIII. The BMD and bone volume fraction (BV/TV) were determined by the CTAn program and the results were shown in Figure 8D,E. Both parameters on Mg/Ag−PIII and Mg−PIII were apparently larger than those on the other two samples ($p < 0.01$) and in particular, Mg/Ag−PIII obtained the largest relative bone volume (BV/TV) ($p < 0.01$).

The histological sections stained by van Gieson's picrofuchsin staining assay were observed. There was little new bone around the pure Ti implant, while all the PIII-treated groups promoted bone formation (Figure 9A). The bone/implant spaces of the pure Ti and Ag−PIII groups were larger than that of the Mg−PIII and Mg/Ag−PIII. The new bone amount and bone/implant contact (BIC) were evaluated quantitatively

DOI: 10.1021/acsami.5b04168
ACS Appl. Mater. Interfaces 2015, 7, 17826−17836

(Figure 9B,C). Consistent with the micro-CT and sequential fluorescent labeling results (Figure 8), the percentage of new bone area around Mg/Ag−PIII group was 93.5 ± 2.93%, which was significantly larger than that around the Mg−PIII (62.53 ± 7.1%, $p < 0.05$), Ag−PIII (37.17 ± 3.26%, $p < 0.01$), and pure Ti (10.9 ± 1.9%, $p < 0.01$) groups. The Mg−PIII group obtained a smaller new bone area than that for the Mg/Ag−PIII group, but both had similar BIC rates, which were significantly larger than those of the Ag−PIII and pure Ti groups. The aforementioned results fully evidenced the synergetic effects of Mg and Ag on osteogenesis and disinfection and the superiority of Mg/Ag dual-source plasma immersion ion implantation (Mg/Ag−PIII) over simultaneously enhancing the osteogenic and antibacterial properties of titanium.

4. DISCUSSION

Osseointegration and antibacterial capability play a critical role in the success of orthopedic and dental implants,[4] and the surface composition of the biomaterials is an important factor.[1] In this study, Mg, Ag, or both were incorporated into Ti, and our in vitro and in vivo results demonstrated that their effects on osteogenesis and disinfection were different. Because silver, magnesium, and spontaneously formed titanium oxide on titanium have distinctive standard electrode potentials (0.7996, −2.363, and −0.502 V, respectively), galvanic corrosion likely occurred over the PIII-treated groups when they were immersed in a physiological medium. This effect controlled release manners of the doped materials (Mg or/and Ag) over PIII groups, which shown that the Ag released by Mg/Ag−PIII was less than that by Ag−PIII (Figure 2B), but the Mg released by Mg/Ag−PIII was more than that by Mg−PIII (Figure 2C). And the Mg/Ag−PIII group demonstrated reliable activities against both *E. coli* and *S. aureus*, and enhanced osteogenic property.

Compared to Ag−PIII group, the antibacterial capability of Mg/Ag−PIII group against the adherent bacteria was also improved. According to ICP-AES, less than 0.05 ppm of Ag was leached from the samples (2 cm squares) after immersion for 28 days, indicated that Ag−PIII and Mg/Ag−PIII groups did not act against bacteria via a Ag-releasing manner, which was consistent with our previous studies.[22,24] Because the standard electrode potential of silver (0.7996 V) is significantly different from that of titanium (−1.630 V) and magnesium (−2.363 V), galvanic corrosion likely occurred over the Ag−PIII and Mg/Ag−PIII groups, in which Ag NPs served as cathodes that stimulate reactions could consume the protons around and disrupt the transmembrane-proton electrochemical-gradient-driven ATP synthesis of bacterial cells.[24,36,37] Because magnesium is more reactive than titanium, the anodic reaction in Mg/Ag system could be stronger than that in the Ti/Ag system. Therefore, the overall efficacy of galvanic corrosion over Mg/Ag−PIII is likely higher than that over Ag−PIII, so does consuming rate of proton and the antibacterial rate of Mg/Ag−PIII group. Further study should be done to reveal the molecular mechanism.

Osteogenesis is another important issue for orthopedic and dental implants. Mesenchymal stem cells (MSCs) are the key repair cells, and their cellular response such as attachment and spreading state on the implant surface is essential to bone healing and implant osseointegration.[38] Because the Ag NPs were immobile on titanium and Ag leakage was little (previously, we found the minimum safe concentration of silver ions for hMSCs was 2 μg/mL,[22] which was 40 fold higher than the peak concentration released by Mg/Ag−PIII or Ag−PIII), the Ag−PIII and Mg/Ag−PIII groups did not exhibit obvious cytotoxicity as shown by the CCK-8 assay (Figure 3D). In addition, it has been shown that Mg plays an essential role in the binding interactions between the integrin family of cell surface receptors and their ligand proteins, resulting in the enhancement of cell attachment and beneficial effects during the initial stage of the bone response.[39−41] In the present study, it was found that Mg enhanced the proliferation of the hBMSCs. The Mg in Mg−PIII and Mg/Ag−PIII was good for the initial adhesion and spreading of hBMSCs. Moreover, after culturing for 1 h, more cells were observed on Mg/Ag−PIII than that on Mg−PIII. The early adhesion and proliferation of hBMSCs could benefit the osteogenic performance of Mg/Ag−PIII at early stage. It was also found that the in vitro and in vivo osteogenic property of Mg/Ag−PIII was better than that of Mg−PIII, especially in the early phase. As an early marker of osteogenic process, the expression level of ALP was higher on Mg/Ag−PIII. More bone formation can be observed on the Mg/Ag−PIII implant surface during the first two weeks in vivo. The better osteogenic performance of Mg/Ag−PIII could be attributed to the aforementioned microgalvanic effect between Ag and Mg. Because the standard electrode potential of silver (0.7996 V) is significantly different from that of magnesium (−2.363 V), the corrosion process (ion releasing) over the Mg/Ag−PIII groups was likely governed by the galvanic effect, in which Mg acted as anode but Ag NPs served as cathodes. Therefore, as we previously proposed,[24] the anodic reactions facilitated the release of Mg, and the cathodic reactions over Ag NPs limited the release of silver ions but consumed the protons around that further influenced the viability of bacteria and the differentiation of hMSCs in different manners, resulting in enhanced osteogenesis of hMSCs on Mg/Ag−PIII.

5. CONCLUSION

To simultaneously enhance the osteogenic activity and antibacterial property, we introduced both silver and magnesium onto the surface of titanium by using the dual-sourced plasma immersion ion implantation (PIII). The in vitro and in vivo results evidenced that the antibacterial and osteogenic properties of the Mg and Ag dual plasma treated group (Mg/Ag−PIII) were better than that of single plasma treated groups (Ag−PIII or Mg−PIII). It was believed that the galvanic effects between Mg and Ag NPs played a key role in controlling the release manners of Mg and Ag, answering for the different biological performances among the concerned sample groups. This study demonstrated that the integration of multiple functional elements can be realized by the dual-sourced PIII technique, and in this case, both the antibacterial properties and osteogenic capability of titanium can be improved. The technique is promising for clinical applications.

■ ASSOCIATED CONTENT

Supporting Information

The Supporting Information is available free of charge on the ACS Publications website at DOI: 10.1021/acsami.5b04168.

List of abbreviations and symbols used in this article; antibacterial property against planktonic bacteria after 24 h of incubation with bacteria (10^7 CFUml^{-1}) evaluated by Live/Dead staining and spread plate method. (PDF)

DOI: 10.1021/acsami.5b04168
ACS Appl. Mater. Interfaces 2015, 7, 17826−17836

AUTHOR INFORMATION

Corresponding Authors

*E-mail: zhangxianl197826@163.com.
*E-mail: xyliu@mail.sic.ac.cn.

Author Contributions

[‖]The manuscript was written through contributions of all authors. All authors have given approval to the final version of the manuscript. These authors contributed equally.

Notes

The authors declare no competing financial interest.

ACKNOWLEDGMENTS

Financial support from the National Basic Research Program of China (973 Program, 2012CB933600), the National Natural Science Foundation of China (81301571, 81472109, and 31370962), the Interdisciplinary (Engineering−Medical) Research Fund of Shanghai Jiao Tong University (YG2011MS30), the Shanghai Committee of Science and Technology, China (14XD1403900), the Opening Project of State Key Laboratory of High Performance Ceramics and Superfine Microstructure (SKL201206SIC), the Fund for Distinguished Young Doctors from Shanghai Municipal Commission of Health and Family Planning (2014), the Youth Innovation Promotion Association CAS (2012196 and 2015204), the Shanghai Rising-Star Program (15QA1404100), the Open Research Fund of State Key Laboratory of Bioelectronics, Southeast University, City University of Hong Kong Strategic Research Grant (SRG) No. 7004188, and the Hong Kong Research Grants Council (RGC) General Research Funds (GRF) CityU No. 112212 are acknowledged.

REFERENCES

(1) Liu, X.; Chu, P. K.; Ding, C. Surface Modification of Titanium, Titanium Alloys, and Related Materials for Biomedical Applications. *Mater. Sci. Eng., R* **2004**, *47*, 49−121.

(2) Zhang, W.; Wang, G.; Liu, Y.; Zhao, X.; Zou, D.; Zhu, C.; Jin, Y.; Huang, Q.; Sun, J.; Liu, X.; Jiang, X.; Zreiqat, H. The Synergistic Effect of Hierarchical Micro/nano-topography and Bioactive Ions for Enhanced Osseointegration. *Biomaterials* **2013**, *34*, 3184−3195.

(3) Neoh, K. G.; Hu, X.; Zheng, D.; Kang, E. T. Balancing Osteoblast Functions and Bacterial Adhesion on Functionalized Titanium Surfaces. *Biomaterials* **2012**, *33*, 2813−2822.

(4) Goodman, S. B.; Yao, Z.; Keeney, M.; Yang, F. The Future of Biologic Coatings for Orthopaedic Implants. *Biomaterials* **2013**, *34*, 3174−3183.

(5) Landi, E.; Tampieri, A.; Mattioli-Belmonte, M.; Celotti, G.; Sandri, M.; Gigante, A.; Fava, P.; Biagini, G. Biomimetic Mg- and Mg,CO3-substituted Hydroxyapatites: Synthesis Characterization and In Vitro Behaviour. *J. Eur. Ceram. Soc.* **2006**, *26*, 2593−2601.

(6) Gronowicz, G.; McCarthy, M. B. Response of Human Osteoblasts to Implant Materials: Integrin-mediated Adhesion. *J. Orthop. Res.* **1996**, *14*, 878−887.

(7) Rezania, A.; Healy, K. E. Integrin Subunits Responsible for Adhesion of Human Osteoblast-like Cells to Biomimetic Peptide Surfaces. *J. Orthop. Res.* **1999**, *17*, 615−623.

(8) Kim, B. S.; Kim, J. S.; Park, Y. M.; Choi, B. Y.; Lee, J. Mg Ion Implantation on SLA-treated Titanium Surface and Its Effects on the Behavior of Mesenchymal Stem Cell. *Mater. Sci. Eng., C* **2013**, *33*, 1554−1560.

(9) Kim, S. R.; Lee, J. H.; Kim, Y. T.; Riu, D. H.; Jung, S. J.; Lee, Y. J.; Chung, S. C.; Kim, Y. H. Synthesis of Si, Mg Substituted Hydroxyapatites and Their Sintering Behaviors. *Biomaterials* **2003**, *24*, 1389−1398.

(10) TenHuisen, K. S.; Brown, P. W. Effects of Magnesium on The Formation of Calcium-deficient Hydroxyapatite from CaHPO4 Center Dot 2H(2)O and Ca-4(PO4)(2)O. *J. Biomed. Mater. Res.* **1997**, *36*, 306−314.

(11) Park, J. W.; An, C. H.; Jeong, S. H.; Suh, J. Y. Osseointegration of Commercial Microstructured Titanium Implants Incorporating Magnesium: a Histomorphometric Study In rabbit Cancellous Bone. *Clin. Oral. Implan. Res.* **2012**, *23*, 294−300.

(12) Janning, C.; Willbold, E.; Vogt, C.; Nellesen, J.; Meyer-Lindenberg, A.; Windhagen, H.; Thorey, F.; Witte, F. Magnesium Hydroxide Temporarily Enhancing Osteoblast Activity and Decreasing the Osteoclast Number in Peri-implant Bone Remodelling. *Acta Biomater.* **2010**, *6*, 1861−1868.

(13) Galli, S.; Naito, Y.; Karlsson, J.; He, W.; Miyamoto, I.; Xue, Y.; Andersson, M.; Mustafa, K.; Wennerberg, A.; Jimbo, R. Local Release of Magnesium from Mesoporous TiO_2 Coatings Stimulates the Peri-implant Expression of Osteogenic Markers and Improves Osteoconductivity in Vivo. *Acta Biomater.* **2014**, *10*, 5193−5201.

(14) Rude, R. K.; Gruber, H. E.; Wei, L. Y.; Frausto, A.; Mills, B. G. Magnesium Deficiency: Effect on Bone and Mineral Metabolism in the Mouse. *Calcif. Tissue Int.* **2003**, *72*, 32−41.

(15) Roy, M.; Fielding, G. A.; Beyenal, H.; Bandyopadhyay, A.; Bose, S. Mechanical, in Vitro Antimicrobial, and Biological Properties of Plasma-sprayed Silver-doped Hydroxyapatite coating. *ACS Appl. Mater. Interfaces* **2012**, *4*, 1341−1349.

(16) Agarwal, A.; Weis, T. L.; Schurr, M. J.; Faith, N. G.; Czuprynski, C. J.; McAnulty, J. F.; Murphy, C. J.; Abbott, N. L. Surfaces Modified with Nanometer-thick Silver-impregnated Polymeric Films that Kill Bacteria But Support Growth of Mammalian Cells. *Biomaterials* **2010**, *31*, 680−690.

(17) De Jong, W. H.; Van Der Ven, L. T.; Sleijffers, A.; Park, M. V.; Jansen, E. H.; Van Loveren, H.; Vandebriel, R. J. Systemic and Immunotoxicity of Silver Nanoparticles in an Intravenous 28 days Repeated Dose Toxicity Study in Rats. *Biomaterials* **2013**, *34*, 8333−8343.

(18) Taglietti, A.; Arciola, C. R.; D'Agostino, A.; Dacarro, G.; Montanaro, L.; Campoccia, D.; Cucca, L.; Vercellino, M.; Poggi, A.; Pallavicini, P.; Visai, L. Antibiofilm Activity of a Monolayer of Silver Nanoparticles Anchored to an Amino-silanized Glass Surface. *Biomaterials* **2014**, *35*, 1779−1788.

(19) Austin, L. A.; Ahmad, S.; Kang, B.; Rommel, K. R.; Mahmoud, M.; Peek, M. E.; El-Sayed, M. A. Cytotoxic Effects of Cytoplasmic-targeted and Nuclear-targeted Gold and Silver Nanoparticles in HSC-3 Cells - a Mechanistic Study. *Toxicol. In Vitro* **2015**, *29*, 694−705.

(20) Singh, R. P.; Ramarao, P. Cellular Uptake, Intracellular Trafficking and Cytotoxicity of Silver Nanoparticles. *Toxicol. Lett.* **2012**, *213*, 249−259.

(21) AshaRani, P. V.; Low Kah Mun, G.; Hande, M. P.; Valiyaveettil, S. Cytotoxicity and Genotoxicity of Silver Nanoparticles in Human Cells. *ACS Nano* **2009**, *3*, 279−290.

(22) Qin, H.; Cao, H.; Zhao, Y.; Zhu, C.; Cheng, T.; Wang, Q.; Peng, X.; Cheng, M.; Wang, J.; Jin, G.; Jiang, Y.; Zhang, X.; Liu, X.; Chu, P. K. In Vitro and In Vivo Anti-biofilm Effects of Silver Nanoparticles Immobilized on Titanium. *Biomaterials* **2014**, *35*, 9114−9125.

(23) Qin, H.; Cao, H.; Zhao, Y.; Jin, G.; Cheng, M.; Wang, J.; Jiang, Y.; An, Z.; Zhang, X.; Liu, X. Antimicrobial and Osteogenic Properties of Silver-ion-implanted Stainless steel. *ACS Appl. Mater. Interfaces* **2015**, *7*, 10785−94.

(24) Cao, H.; Liu, X.; Meng, F.; Chu, P. K. Biological Actions of Silver Nanoparticles Embedded in Titanium Controlled by Micro-galvanic Effects. *Biomaterials* **2011**, *32*, 693−705.

(25) Cao, H.; Cui, T.; Jin, G.; Liu, X. Cellular Responses to Titanium Successively Treated by Magnesium and Silver PIII&D. *Surf. Coat. Technol.* **2014**, *256*, 9−14.

(26) Anders, A. *Handbook of Plasma Immersion Ion Implantation and Deposition*. John Wiley & Sons, Ltd.: New York, 2000.

(27) Wang, S.; Zhang, Z.; Zhao, J.; Zhang, X.; Sun, X.; Xia, L.; Chang, Q.; Ye, D.; Jiang, X. Vertical Alveolar Ridge Augmentation with Beta-tricalcium Phosphate and Autologous Osteoblasts in Canine Mandible. *Biomaterials* **2009**, *30*, 2489−2498.

DOI: 10.1021/acsami.5b04168
ACS Appl. Mater. Interfaces 2015, 7, 17826−17836

(28) Zhao, J.; Shen, G.; Liu, C.; Wang, S.; Zhang, W.; Zhang, X.; Zhang, X.; Ye, D.; Wei, J.; Zhang, Z.; Jiang, X. Enhanced Healing of Rat Calvarial Defects with Sulfated Chitosan-coated Calcium-deficient Hydroxyapatite/bone Morphogenetic Protein 2 Scaffolds. *Tissue Eng., Part A* **2012**, *18*, 185−197.
(29) Monteiro, O. R.; Wang, Z.; Brown, I. G. Deposition of Mullite and Mullite-like Coatings on Silicon Carbide by Dual-source Metal Plasma Immersion. *J. Mater. Res.* **1997**, *12*, 2401−2410.
(30) Anders, A. Plasma and Ion Sources in Large Area Coating: A review. *Surf. Coat. Technol.* **2005**, *200*, 1893−1906.
(31) Wynblatt, P. Interfacial Segregation Effects inWetting Phenomena. *Annu. Rev. Mater. Res.* **2008**, *38*, 173−96.
(32) Jerome, R.; Teyssie, P.; Pireaux, J. J.; Verbist, J. J. Surface Analysis of Polymers End-capped with Metal Carboxylates Using X-ray Photoelectron Spectroscopy. *Appl. Surf. Sci.* **1986**, *27*, 93−105.
(33) Bird, R. J.; Swift, P. Energy Calibration in Electron Spectroscopy and The Re-determination of Some Reference Electron Binding Energies. *J. Electron Spectrosc. Relat. Phenom.* **1980**, *21*, 227−240.
(34) Fuggle, J.; Källne, E.; Watson, L.; Fabian, D. Electronic Structure of Aluminum and Aluminum-noble-metal Alloys Studied by Soft-x-ray and X-ray Photoelectron Spectroscopies. *Phys. Rev. B: Condens. Matter Mater. Phys.* **1977**, *16*, 750−761.
(35) Li, J.; Qiao, Y.; Ding, Z.; Liu, X. Microstructure and Properties of Ag/N Dual Ions Implanted Titanium. *Surf. Coat. Technol.* **2011**, *205*, 5430−5436.
(36) Boyer, P. D. The ATP Synthase - A Splendid Molecular Machine. *Annu. Rev. Biochem.* **1997**, *66*, 717−749.
(37) von Ballmoos, C. Alternative Proton Binding Mode in ATP Synthases. *J. Bioenerg. Biomembr.* **2007**, *39*, 441−445.
(38) Razzouk, S.; Schoor, R. Mesenchymal Stem Cells and Their Challenges for Bone Regeneration and Osseointegration. *J. Periodontol.* **2012**, *83*, 547−550.
(39) Zreiqat, H.; Howlett, C. R.; Zannettino, A.; Evans, P.; Schulze-Tanzil, G.; Knabe, C.; Shakibaei, M. Mechanisms of Magnesium-stimulated Adhesion of Osteoblastic Cells to Commonly Used Orthopaedic Implants. *J. Biomed. Mater. Res.* **2002**, *62*, 175−184.
(40) Leem, Y. H.; Lee, K. S.; Kim, J. H.; Seok, H. K.; Chang, J. S.; Lee, D. H. Magnesium Ions Facilitate Integrin alpha 2- and alpha 3-mediated Proliferation and Enhance Alkaline Phosphatase Expression and Activity In hBMSCs. *J. Tissue Eng. Regener. Med.* **2014**, n/a.
(41) Zreiqat, H.; Valenzuela, S. M.; Nissan, B. B.; Roest, R.; Knabe, C.; Radlanski, R. J.; Renz, H.; Evans, P. J. The Effect of Surface Chemistry Modification of Titanium Alloy on Signalling Pathways in Human Osteoblasts. *Biomaterials* **2005**, *26*, 7579−7586.

DOI: 10.1021/acsami.5b04168
ACS Appl. Mater. Interfaces 2015, 7, 17826−17836